

Numerical Optimization of Dy-Doped ZBLAN Fiber Lasers for Yellow Emission

Michelangelo Federico , Graduate Student Member, IEEE, and Federica Poli , Member, IEEE

Abstract—Lasers operating within the yellow range of the visible spectrum are widely adopted in many fields, ranging from astronomy to medicine, particularly for the safe treatment of macular retinopathy. The interest in Dysprosium-doped Fiber Lasers (FLs) is growing due to advances in blue pump laser diodes and high-quality fluoride fibers, to be used as the active medium, with the promise of cost-effective, compact and reliable yellow emission. In this study a matrix-based model based on rate equations is used to thoroughly investigate the impact of Excited State Absorption (ESA) on the performance of tunable yellow FLs, revealing its significant effect on efficiency and tunability. Additionally, the potential of mid-infrared cascade lasing to mitigate ESA effects was investigated. Results provide insights into the enhancing of the output power behaviour of yellow FL sources through careful selection of output mirror reflectivity and active fiber length. This work anticipates significant improvements in the achievable performance via cascade lasing, paving the way for future experimental validation.

Index Terms—Fiber laser, yellow lasing, tunable lasers, excited state absorption, dysprosium-doped fluoride fiber, MIR cascade lasing, rate equations modeling, numerical optimization.

I. INTRODUCTION

YELLOW lasers operating within the visible spectrum from 565 nm to 590 nm have demonstrated various advantages for applications in numerous fields such as astronomy, microscopy, material processing, scientific research, biology and medicine [1], [2], [3], [4], [5]. In particular, lasing in the yellow range is highly promising for the treatment of ophthalmologic and dermatologic diseases due to its effective interaction with human tissues based on their absorption characteristics [3], [4], [5]. In fact, 577 nm is considered the wavelength choice for macular retinopathy treatment via photocoagulation of oxyhemoglobin, as it offers a perfect combination of low absorption by both the retinal and foveal pigments, and high absorption from oxyhemoglobin [6]. This coincidence, together with a low scattering by the eye tissue, paves the way to central macular edema treatments with lower risk of affecting the patient's vision. Nevertheless, commercially available yellow sources, based on non-linear frequency conversion [7] or dye lasers [4],

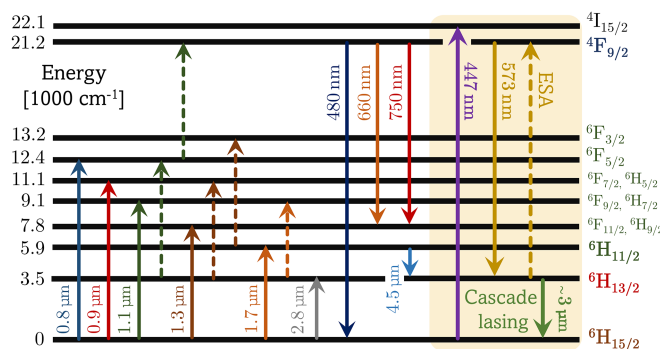


Fig. 1. General Dy³⁺ energy level diagram showing various transitions. Those for yellow and MIR lasing are highlighted in the yellow area.

are still complex, expensive, and usually have low efficiency and reliability. In this framework, the interest in yellow Fiber Lasers (FLs) has greatly increased alongside the improvement of blue GaN pump laser diodes [8], as well as the recent fabrication of fibers made of high-quality, low loss, fluoride glasses, to be used as the active medium [9]. Compared to the widely adopted silica glass, fluoride ones offer a lower phonon energy, needed for Mid-InfraRed (MIR) emission, and better loss characteristics in the visible spectrum [10]. Although fluoride glass processing is still challenging, high-quality components, like combiners [11] and Fiber Bragg Gratings (FBGs) [12], [13], [14], [15], have been demonstrated. Moreover, fibers made with ZBLAN and fluoroindate glasses, doped with different rare-earth elements, have been used for high-efficiency lasers emitting in the MIR range [14], [15], [16], [17], [18], [19], [20], [21]. These FLs hold promise for providing cost-effective, compact, and reliable emission, delivering excellent performance not only in the MIR spectrum but also in the visible one.

In this regard, Dysprosium (Dy) is the best candidate for yellow emission [22]. As shown in Fig. 1, Dy³⁺ rare earth ions offer the ⁴F_{9/2} energy level with relatively long lifetime, that can be directly accessed by several excitation wavelengths from ultra-violet to visible range, and from which different visible emission transitions are possible. Moreover, yellow emission from Dy turns out to be a classical 4-level lasing system with a potential Stokes efficiency as high as 78%. These factors made blue-pumped Dy:ZBLAN FLs for yellow emission a real possibility worth investigating, and are lately gaining a lot of attention from the research community. The ⁴F_{9/2} → ⁶H_{13/2} transition of Dy³⁺ has latterly been exploited to experimentally demonstrate different types of yellow ZBLAN FLs via pumping

Manuscript received 18 October 2023; revised 1 December 2023; accepted 7 December 2023. Date of publication 13 December 2023; date of current version 2 April 2024. (Corresponding author: Michelangelo Federico.)

The authors are with the Department of Engineering and Architecture, University of Parma, I-43124 Parma, Italy (e-mail: michelangelo.federico@unipr.it; federica.poli@unipr.it).

Color versions of one or more figures in this article are available at <https://doi.org/10.1109/JLT.2023.3342288>.

Digital Object Identifier 10.1109/JLT.2023.3342288

at $\simeq 450$ nm. J. Zou, et al. demonstrated Watt-level fiber lasing with a central wavelength of 575 nm [23], whereas H. Wang, et al. succeeded in obtaining stable tunability in the range from 568.7 nm to 581.9 nm [24]. However, M. Z. Amin, et al. showed both experimentally and theoretically that the Excited State Absorption (ESA) from the lower lasing level ${}^6\text{H}_{13/2}$ to the higher one ${}^4\text{F}_{9/2}$ can negatively affect the slope efficiency of these types of lasers. This is due to the relatively high lifetime of the ${}^6\text{H}_{13/2}$ level compared to that of the ${}^4\text{F}_{9/2}$ one [25], and it is a direct consequence of the lower phonon energy of fluoride glasses, especially ZBLAN. Cascade lasing at $3\ \mu\text{m}$ through the ${}^6\text{H}_{13/2} \rightarrow {}^6\text{H}_{15/2}$ transition was proposed to mitigate this effect via the depopulation of the ${}^6\text{H}_{13/2}$ level [22]. While there is a numerical analysis regarding the impact of ESA on tunable yellow FLs [26] and a preliminary study of the positive effect of cascade lasing [27], literature still lacks a comprehensive examination of both aspects. Such an investigation would provide key design insights for enhancing the performance of yellow FL sources.

In this work, a matrix-based model based on rate equations was applied to intensively examine the influence of ESA on the performance of tunable yellow FLs. Moreover, cascade lasing in the MIR was optimized to improve emission in the yellow range. After a successful calibration of the model based on the most recent experimental work, the tunability and efficiency of yellow Dy-doped FLs were studied as a function of pump power, cavity length and reflectivity of the output mirror both with and without cascade lasing. Results revealed the extremely positive impact given by cascade lasing in counteracting the negative influence of ESA and saturation effects at elevated input pump power, both due to the long lifetime of the ${}^6\text{H}_{13/2}$ level. These findings hint at potential improvements in output power and tunability performance that go beyond what previous studies have explored [26].

II. MATRIX-BASED MODEL

The matrix-based rate equation model used in the present study was developed by implementing the theory reported by R. I. Woodward and M. Gorjan in [17], [28], to simulate FLs. Rate equations are widely used for numerical analyses of various types of lasers, but existing commercial and open-source software commonly lacks versatility and adaptability, respectively. Our implementation allows us to deeply understand the system's behaviour by directly modifying the source code, without any fundamental constraints. Moreover, the matrix-based approach is adaptable to various rate equation systems without the need for time-consuming equation solving or extensive code modifications. The model, which is extremely general and complete, is easily adaptable to any type of fiber and dopant, regardless of the number of energy levels, once all the spectroscopic data and input parameters are available.

With the model, it is possible to determine the power at any wavelength and the population of every level along the fiber by iteratively solving power flow (1) and population rate equations (2), considering boundary conditions set by the mirrors at both ends of the fiber. In the most general case, the power evolution

along the fiber (z) for each channel of wavelength λ , for both signals and pumps, forward (+) and backward (−) propagating, is expressed as [28]:

$$\frac{dP^\pm(\lambda, z)}{dz} = \pm P^\pm(\lambda, z) \times \left[\Gamma(\lambda) \sum_{i,j (i>j)} (\sigma_{ij}(\lambda)N_i(z) - \sigma_{ji}(\lambda)N_j(z)) - \alpha(\lambda) \right] \quad (1)$$

where Γ is the doped core overlap factor, α the fiber background loss, and σ_{ij} the absorption ($i < j$) and emission ($i > j$) cross-sections between levels i and j . The population rate equations are expressed in matrix form as [28]:

$$\frac{d\mathbf{N}}{dt} = \mathbf{L}\mathbf{N} + \mathbf{K} \quad (2)$$

where \mathbf{L} and \mathbf{K} are matrices which describe the linear and nonlinear population change rate terms, respectively, and $\mathbf{N} = [N_0, N_1, \dots, N_{l-1}]$ is a vector containing the population of every level, from the ground state 0 up to the highest level $l - 1$. In this work, the linear matrix is represented as the sum of two matrices $\mathbf{L} = \mathbf{L}^c + \mathbf{L}^p$, with:

$$\mathbf{L}^c = \begin{bmatrix} 0 & \mathbf{R}_{10} & \cdots & \mathbf{R}_{(l-1)0} \\ 0 & -\sum_{i=0}^1 \mathbf{R}_{1i} & \cdots & \mathbf{R}_{(l-1)1} \\ \vdots & \vdots & \ddots & \vdots \\ 0 & 0 & \cdots & -\sum_{i=0}^{l-1} \mathbf{R}_{(l-1)i} \end{bmatrix} \quad (3)$$

$$\mathbf{L}^p = \begin{bmatrix} -\sum_{i=0}^{l-1} \mathbf{W}_{0i} & \mathbf{W}_{10} & \cdots & \mathbf{W}_{(l-1)0} \\ \mathbf{W}_{01} & -\sum_{i=0}^{l-1} \mathbf{W}_{1i} & \cdots & \mathbf{W}_{(l-1)1} \\ \vdots & \vdots & \ddots & \vdots \\ \mathbf{W}_{0(l-1)} & \mathbf{W}_{1(l-1)} & \cdots & -\sum_{i=0}^{l-1} \mathbf{W}_{(l-1)i} \end{bmatrix} \quad (4)$$

where $R_{ij} = A_{ij} + W_{ij}^{nr}$, $A_{ij} = \beta_{ij}/\tau_i^r$ and $W_{ij}^{nr} = 1/\tau_i^{nr}$ describing the spontaneous emission (zero if $i < j$) and the non-radiative transitions (zero if $i \neq j + 1$). W_{ij} are the absorption ($i < j$) and stimulated emission ($i > j$) rates. Here τ_i^{nr} and τ_i^r are the nonradiative and radiative lifetime of level i , and β_{ij} the branching ratio between levels i and j . The matrix splitting is crucial for numerical modelling as the contribution of \mathbf{L}^c can be pre-computed based on known input parameters, whereas terms in \mathbf{L}^p depend on the power along the fiber and take part in the active solving procedure. In this study, the focus was on continuous wave laser behaviour, with (1) being solved in steady-state regime. Furthermore, nonlinear transfer processes, like energy transfer and cross relaxation, were negligible, resulting in setting \mathbf{K} in (2) to zero.

III. INPUT PARAMETERS

Solving the equations in Section II requires knowledge of fiber and cavity properties, emission and absorption cross-section

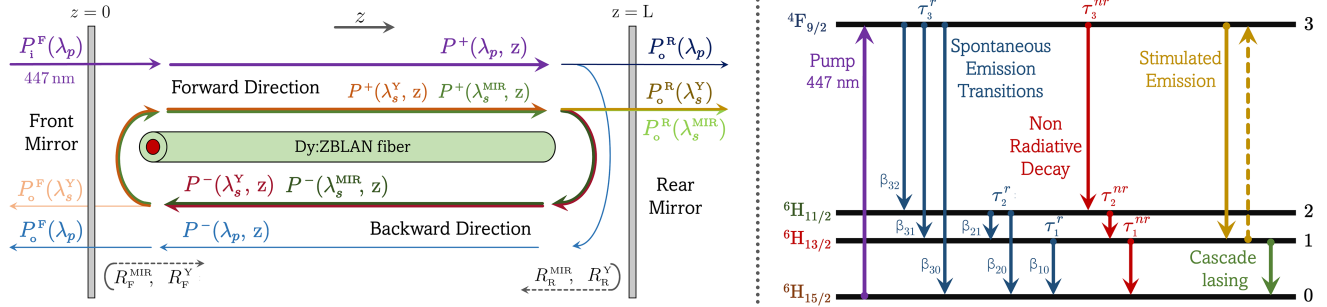


Fig. 2. (Left): FL cavity scheme considered in this simulation work. (Right): Dy^{3+} energy level diagram showing the main transitions.

spectra, radiative and nonradiative lifetimes vectors, and the branching ratios matrix. These input parameters were carefully gathered from literature [17], [18], [22], [25] and finely tuned by mirroring the methodology employed by Amin et al. in their analysis [22] to accurately match the results of the most recent works, both theoretical and experimental [16], [22], [23], [24]. This approach is essential to mitigate the inherent uncertainties associated with experimental measurements and the approximation errors of theoretical calculations, ensuring a robust foundation of parameters to be used for numerical simulations. The following sections detail all the input parameters utilized in our simulations.

A. Fiber Properties and Laser Design

The linear cavity setup, illustrated in Fig. 2 (left), was built up by a Dy:ZBLAN fiber made by Le Verre Fluoré. The fiber is single-cladding with a core radius of $6.25 \mu\text{m}$, a numerical aperture of 0.16, and a Dy ion concentration in the core of $3.68 \times 10^{26} \text{m}^{-3}$. Although the manufacturer states a background loss of approximately 0.04 dB/m at the yellow lasing wavelength and even lower for the MIR range, higher values resulted more in line with experimental results [22]. The attenuation was set to 0.18 dB/km and 0.17 dB/km at the blue pump and yellow signal wavelength [22], and to the values reported in [18] at the MIR one. Overlap factors were calculated as 0.9846 for the pump at 447 nm, in the range $0.9846 \div 0.9837$ for signals in the yellow band ($555 \div 595 \text{ nm}$), and in the range $0.7401 \div 0.6572$ for MIR signals ($3 \div 3.4 \mu\text{m}$), using the expression for uniformly doped cores [29] and Marcuse's equation [30] to estimate the mode field diameter.

B. Cross-Sections, Lifetimes and Branching Ratios

Emission and absorption cross-sections are extremely important to calculate the W_{ij} rates. Fig. 3 shows the re-digitized spectra of both absorption and emission cross-section of the ${}^4\text{F}_{9/2} \leftrightarrow {}^6\text{H}_{13/2}$ and ${}^6\text{H}_{13/2} \leftrightarrow {}^6\text{H}_{15/2}$ signal transitions [18], [22]. The pump absorption cross-section at 447 nm was set to $3.431 \times 10^{-26} \text{m}^2$ [22].

Lifetimes τ_i^r and τ_i^{nr} , and branching ratios β_{ij} were necessary for calculating W_{ij}^{nr} and A_{ij} rates. For this work, all values were found in literature [17], [22], [25]:

$$\tau^{nr} = \begin{bmatrix} \tau_1^{nr} & \tau_2^{nr} & \tau_3^{nr} \end{bmatrix} = \begin{bmatrix} 650 \mu\text{s} & 1.25 \mu\text{s} & \simeq \infty \end{bmatrix} \quad (5)$$

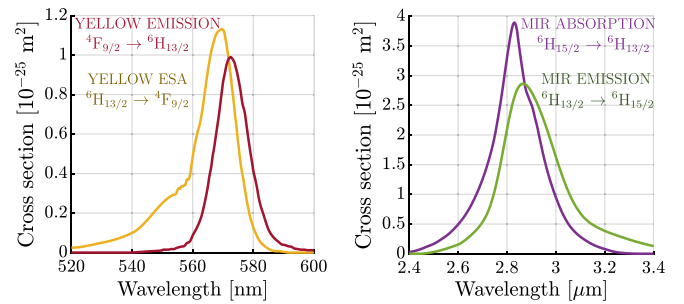


Fig. 3. Absorption and emission cross-sections of the Dy:ZBLAN fiber by Le Verre Fluoré. Spectra for the yellow range (left) sourced from [22] and scaled by 1.11 and 1.24, respectively. Spectra for the MIR range around $3 \mu\text{m}$ (right) directly taken from [18].

$$\tau^r = \begin{bmatrix} \tau_1^r & \tau_2^r & \tau_3^r \end{bmatrix} = \begin{bmatrix} 46.8 \text{ ms} & 13.7 \text{ ms} & 1.5 \text{ ms} \end{bmatrix} \quad (6)$$

$$\beta = \begin{bmatrix} \beta_{10} & \beta_{20} & \beta_{30} \\ 0 & \beta_{21} & \beta_{31} \\ 0 & 0 & \beta_{32} \end{bmatrix} = \begin{bmatrix} 1 & 0.948 & 0.59 \\ 0 & 0.052 & 0.29 \\ 0 & 0 & 0.12 \end{bmatrix} \quad (7)$$

IV. SIMULATION SETUP AND ANALYSES

In this work, the FL scheme used for simulations is a linear cavity with mirrors at both ends, as shown in Fig. 2 (left). The unreflected light at the fiber's rear-end can be taken as the laser output. Reflectivities at the yellow, MIR, and pump wavelengths for front and rear-end mirrors ($R_F^Y, R_F^{\text{MIR}}, R_F^P, R_R^Y, R_R^{\text{MIR}}$ and R_R^P), along with pump power injected at the front-end $P_i^F(\lambda_p)$ and output power at wavelengths in the yellow ($P_o^R(\lambda_s^Y)$) and MIR ($P_o^R(\lambda_s^{\text{MIR}})$) range are key parameters. Tunability was achieved by changing the selected yellow wavelength λ_s^Y within the cavity. This can be done experimentally via a diffraction grating and a mirror in a Littrow configuration [24], usually introducing losses in the system which were not considered in the model. Cascade lasing was obtained by adding a very high-Q cavity at the MIR wavelength. A double cavity can be obtained by adding FBGs operating in the MIR range. Although achieving very high reflectivity values remains challenging in fluoride glasses, these devices have already been successfully demonstrated in both fluoroindate [14], [15] and ZBLAN [13] fibers. Our results, focusing on a low-loss cavity with nearly

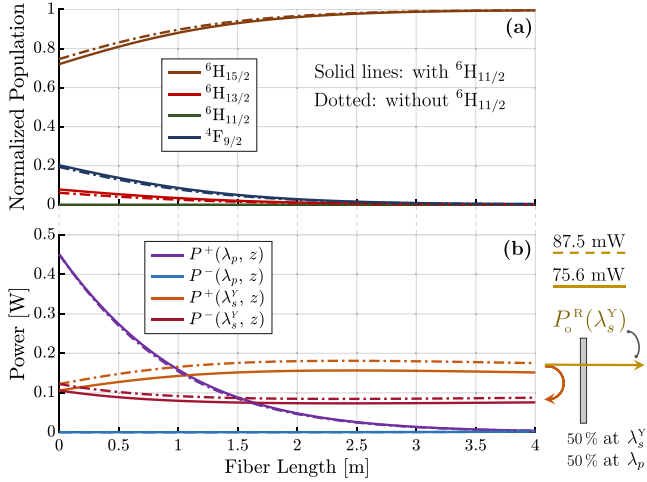


Fig. 4. Level ${}^6\text{H}_{11/2}$ impact on the normalized population distribution (a), and on the evolution of pump and signal power (b) along the doped fiber for $P_1^F(\lambda_p) = 451$ mW, $R_R^Y = R_R^P = 50\%$, $L = 4$ m, and $\lambda_s^Y = 573$ nm [22].

ideal reflectivities, provide valuable insights into the potentially achievable performance with tunable yellow FLs.

A. Energy Level Diagram Simplification

The energy level diagram utilized for the simulations is that in Fig. 2 (right). Although the complete diagram can be easily implemented by the model, it was decided to simplify it as much as possible, without loss of accuracy in the results, to reduce simulation time. The ${}^4\text{I}_{15/2}$ level was removed, since the energy gap with respect to the ${}^4\text{F}_{9/2}$ one is very low, thus making the nonradiative lifetime extremely low. Moreover, since the lasing behaviour is provided by three levels, namely the ground state ${}^6\text{H}_{15/2}$, the upper metastable level ${}^6\text{F}_{9/2}$, and the lower metastable one ${}^6\text{H}_{13/2}$, the diagram was further simplified by clustering all the other levels together into the ${}^6\text{H}_{11/2}$ one, which was seen to be essential to reach accurate results. While the former simplification is widely adopted when modelling lasing behaviour, the latter is a novelty of this work. Fig. 4 illustrates the impact of these simplifications on the normalized population distribution (a), as well as on the pump and signal power (b) along the Dy^{3+} -doped fiber. Beyond showing the working principle of the model, the figure demonstrates that the omission of the ${}^6\text{H}_{11/2}$ level influences the key simulation result, $P_o^R(\lambda_s^Y)$, which increases from 75.6 mW to 87.6 mW. Moreover, it highlights the model's capability to accurately reproduce results in literature [22].

B. Performed Analyses

The laser setup described in the previous sections was used for various simulations, with the aim of analyzing the effects of ESA and the improvement given by MIR cascade lasing on tunable yellow FL performance. Firstly, the influence of the fiber length $L = 0.3 \div 4$ m, and of the rear mirror reflectivity $R_R^Y = 10 \div 90\%$ on $P_o^R(\lambda_s^Y)$ in the wavelength range $\lambda_s^Y = 555 \div 595$ nm as a function of $P_1^F(\lambda_p)$ at 447 nm was

analyzed both with and without the effect of ESA, which was disabled by setting to zero the corresponding cross-section. After evaluating the achievable performance by reducing ESA, a preliminary optimization of cascade lasing was carried out, studying the influence of $L = 0.3 \div 5.5$ m, MIR wavelength $\lambda_s^{\text{MIR}} = 3 \div 3.4$ μm , and $R_R^Y = 10 \div 90\%$ on $P_o^R(\lambda_s^Y)$ at 573 nm as a function of $P_1^F(\lambda_p)$ at 447 nm. Useful information on the optimal L , λ_s^{MIR} , and R_R^Y values were found using four main key performance indicators: the lasing threshold for yellow emission (Th^Y), its slope efficiency before (SI^Y) and after (SI^{CY}) MIR emission, and the threshold of MIR lasing (Th^{MIR}). Finally, the first analysis was repeated by enabling cascade lasing at the optimal wavelength $\lambda_s^{\text{MIR}} = 3.3$ μm , as determined by the results of the previous simulations. Useful guidelines on the optimal length L_{opt} and R_R^Y values to improve the laser tunability and efficiency by introducing an additional MIR cascade cavity are obtained. For all the above mentioned analyses both mirrors were highly transmissive at $\lambda_p = 447$ nm ($R_F^P = 0\%$ and $R_R^P = 1\%$), and the front-end mirror was highly reflective in the yellow spectral range ($R_F^Y = 99.94\%$). Regarding the MIR cavity, both mirrors were highly reflective at λ_s^{MIR} ($R_F^{\text{MIR}} = 100\%$ and $R_R^{\text{MIR}} = 99\%$).

Some insights into the influence of the FBGs reflectivity are also provided by repeating the analysis with λ_s^Y fixed at 573 nm in both the case of a lower R_F^Y of 95%, and that of a non-ideal MIR cavity ($R_F^{\text{MIR}} = 95\%$ and $R_R^{\text{MIR}} = 95\%$).

V. RESULTS AND DISCUSSION

As shown in [26], where we investigated the impact of ESA on the tunable yellow FL for fixed $P_1^F(\lambda_p)$ values, the wavelength λ_{peak}^Y providing the maximum output power is the peak one of the emission spectrum (573 nm), regardless of R_R^Y , when ESA is disabled, whereas it is shifted to a higher value by ESA. The red shift becomes more significant with increasing $P_1^F(\lambda_p)$ and decreasing R_R^Y . Moreover, it was shown that the optimal length L_{opt} is directly proportional to $P_1^F(\lambda_p)$ and inversely proportional to R_R^Y , and it rises as the yellow wavelength λ_s^Y deviates from λ_{peak}^Y , being equal or slightly lower when ESA is considered.

For a broader understanding of ESA impact on the efficiency and tunability of the yellow FL, two key aspects are here presented. In Fig. 5 (bottom) the maximum attainable output power $P_o^R(\lambda_s^Y)$ is plotted versus the input pump power $P_1^F(\lambda_p)$, for various R_R^Y values, both with (a) and without (b) ESA. Notice that each reported $P_o^R(\lambda_s^Y)$ is that at λ_{peak}^Y for different length values, as L_{opt} differs for specific couples of $P_1^F(\lambda_p)$ and R_R^Y values. In Fig. 5 (top) the 3-dB tuning range $T_{3\text{dB}}$ is shown as a function of $P_1^F(\lambda_p)$ for different R_R^Y values, with (a) and without (b) ESA. Note that $T_{3\text{dB}}$ is defined as the wavelength range within which $P_o^R(\lambda_s^Y)$ is at least $P_o^R(\lambda_{\text{peak}}^Y) - 3$ dB. It must be pointed out that the L_{opt} values providing the highest output power is slightly lower than that needed to obtain the best $T_{3\text{dB}}$.

Fig. 5 (bottom) also reveals that higher R_R^Y values lead to lower Th^Y and SI^Y , showing a dependence of the optimal FL's operational regime on the rear mirror reflectivity. A high R_R^Y is preferable at low $P_1^F(\lambda_p)$, whereas a low reflectivity value is favoured at high input power. For instance, the system with

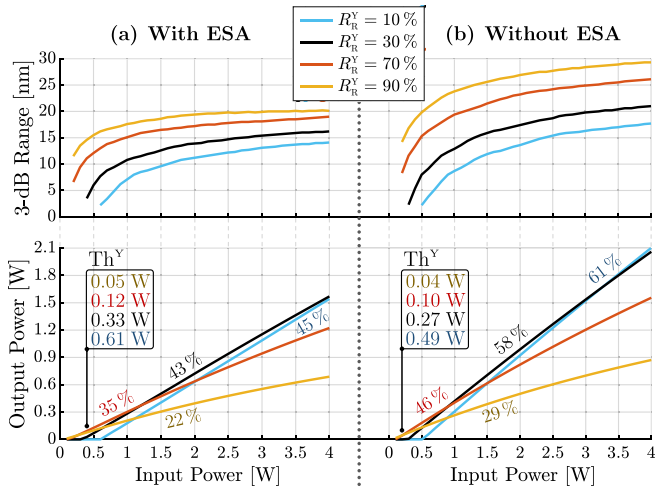


Fig. 5. Maximum achievable $T_{3\text{dB}}$ (top) and $P_0^R(\lambda_s^Y)$ (bottom) versus $P_1^F(\lambda_p)$, for different R_R^Y values, with (a) and without (b) ESA.

ESA achieves a maximum output power of 127 mW for $R_R^Y = 70\%$, when $P_1^F(\lambda_p)$ is set at 500 mW, whereas the maximum output power is 1.57 W for $R_R^Y = 30\%$, when $P_1^F(\lambda_p)$ is set at 4 W. For comparison, the system without ESA provides a maximum output power of 182 mW for $R_R^Y = 70\%$, and 2.1 W for $R_R^Y = 10\%$ when $P_1^F(\lambda_p)$ is set at 500 mW and 4 W, respectively, showing an increase of 43% and 34% in the two cases. Additionally, both with and without ESA, the FL tends to saturate as $P_1^F(\lambda_p)$ increases, particularly with higher R_R^Y , since the optical power inside the cavity rises. Regarding tunability, Fig. 5 (top) shows that $T_{3\text{dB}}$ increases with $P_1^F(\lambda_p)$, and that higher reflectivity R_R^Y values result in a better tunability. The laser tuning range without ESA improves faster as the input power increases and, unlike the system with ESA, it does not flatten inside the simulated range of values. For instance, the best achievable $T_{3\text{dB}}$ when $P_1^F(\lambda_p) = 4$ W and $R_R^Y = 10\%$, with and without ESA, is $\simeq 20$ nm and $\simeq 29$ nm, respectively, providing a 45% improvement. To summarize, it is clear that ESA negatively impacts both efficiency and tunability of the FL, as Th^Y , SI^Y and $T_{3\text{dB}}$ worsen.

It is important to underline that these results, along with those in [26], demonstrate the need to mitigate the ESA effect for improved FL performance in terms of peak power and tuning range. The benefits given by the adoption of cascade lasing are firstly investigated by focusing on yellow emission at 573 nm, in order to carry out a preliminary optimization of the MIR wavelength. In Fig. 6(a), Th^{MIR} is displayed versus λ_s^{MIR} for various R_R^Y and L values, showing that the minimum threshold is consistently achieved at $\lambda_s^{\text{MIR}} = 3.3 \mu\text{m}$. Fig. 6(b) presents the output power of the yellow FL versus $P_1^F(\lambda_p)$ in three conditions, without ESA, and in its presence both without and with cascade lasing, when $\lambda_s^{\text{MIR}} = 3.3 \mu\text{m}$ and $R_R^Y = 50\%$. The fiber length is 4 m, 3.2 m, and 2.1 m, respectively. These values were chosen to provide an overall better performance within the considered range of $P_1^F(\lambda_p)$. In fact, L_{opt} increases with $P_1^F(\lambda_p)$, especially when cascade lasing is not present. Since the FL performance for a certain pump power is more negatively

affected by a fiber which is shorter than L_{opt} , it is preferred to use a longer length. In particular, the chosen L value is close to the optimal one for $P_1^F(\lambda_p) = 4$ W. Notice that with cascade lasing, the yellow emission starts with a low Th^Y value, and its slope efficiency is SI^Y until Th^{MIR} is reached, then it increases to SI^{CY} . Moreover, SI^Y and SI^{CY} are equal to SI^Y in the cases with and without ESA, respectively. Therefore, cascade lasing effectively mitigates ESA. Furthermore, the graph highlights that the FL output power does not saturate when cascade lasing is active. This suggests that the long lifetime of the ${}^6\text{H}_{13/2}$ level also causes saturation at high $P_1^F(\lambda_p)$ by immobilizing active ions. Increasing the fiber length can only alleviate this unwanted effect, whereas cascade lasing effectively eliminates it via the repopulation of the ground state ${}^6\text{H}_{15/2}$. This is supported by the blue dashed curve in Fig. 6(b), which can be obtained either by setting τ_1^{nr} to zero or enabling cascade lasing while disabling ESA.

Based on these findings, it is demonstrated that cascade lasing significantly enhances emission at 573 nm by reducing both ESA and saturation effects due to the long lifetime of the ${}^6\text{H}_{13/2}$ level. Results show that optimization is achieved when $\lambda_s^{\text{MIR}} = 3.3 \mu\text{m}$, as Th^{MIR} reaches its minimum, and that a very high-Q MIR cavity is optimal, as it completely eliminates the negative impact of ESA. A preliminary analysis into the FBGs reflectivity influence on the performance of the FL showed that when R_F^Y is lowered of just 5%, both thresholds Th^Y and Th^{MIR} remain nearly unchanged, regardless of R_R^Y . However, the slope efficiencies SI^Y and SI^{CY} decrease, experiencing a reduction of more than 19% when $R_R^Y = 90\%$ and less than 2% when $R_R^Y = 10\%$. Considering the case of a non-ideal MIR cavity, reducing R_F^{MIR} and R_R^{MIR} to 95% leaves Th^Y and SI^Y unaffected. Nonetheless, the MIR threshold increases, reaching 1.9 W from 1.5 W, and 1.2 W from 0.7 W when R_R^Y is 10% and 90%, respectively. Moreover, the slope efficiency after the MIR threshold remains unchanged, regardless of R_R^Y , proving once again the optimality of the very high-Q cavity.

The following sections investigate the enhancements in FL performance across the entire yellow emission spectrum with cascade lasing enabled at the optimized MIR wavelength value $\lambda_s^{\text{MIR}} = 3.3 \mu\text{m}$, assuming the use of high-quality FBGs.

A. Cascade Lasing Improvement

To provide an overview of the impact on efficiency and tunability of the FL, the analysis at the beginning of Section V was repeated with cascade lasing enabled. Results shown in Fig. 7 still represent the highest achievable output power and tuning range, optimized for the specified parameters, $P_1^F(\lambda_p)$ and R_R^Y . Fig. 7 (bottom) shows that the peak power behaviour aligns with that in Fig. 5 (bottom), regardless of R_R^Y . The maximum achievable power matches that of the case with ESA until the MIR threshold is reached. When $P_1^F(\lambda_p)$ becomes higher than Th^{MIR} , the laser reaches the same slope efficiency as in the case with ESA disabled, but without ever undergoing saturation. Cascade lasing can therefore enhance the FL performance compared to the case when ESA is not considered, especially at high $P_1^F(\lambda_p)$ and low R_R^Y values. In terms of tunability, as shown in

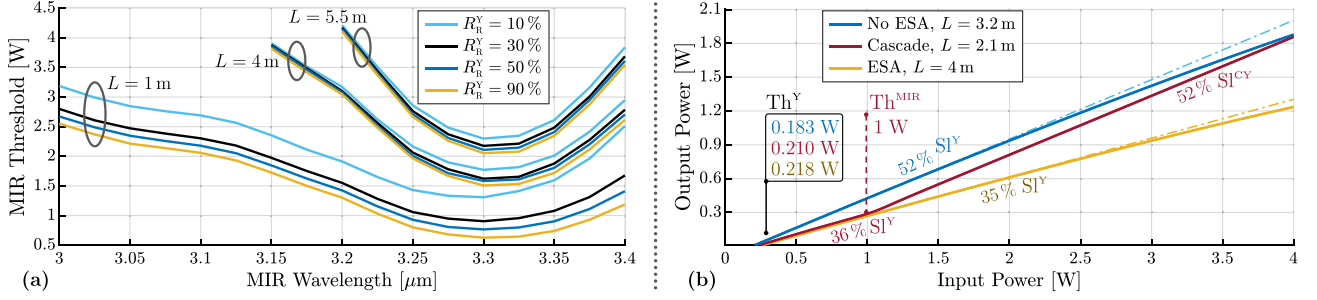


Fig. 6. (a) MIR lasing threshold Th^{MIR} versus λ_s^{MIR} for different R_R^Y and L values. (b) Yellow output power $P_o^R(\lambda_s^Y)$ versus $P_i^F(\lambda_p)$ for $R_R^Y = 50\%$ and $\lambda_s^{\text{MIR}} = 3.3 \mu\text{m}$. Comparison between the cases with and without ESA, and with cascade lasing. The fiber length is 4 m, 3.2 m, and 2.1 m respectively.

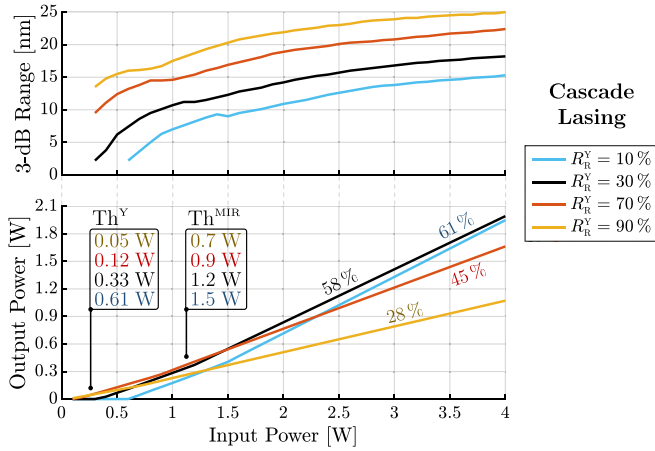


Fig. 7. Maximum achievable $T_{3\text{dB}}$ (top) and $P_o^R(\lambda_s^Y)$ (bottom) versus $P_i^F(\lambda_p)$, for different R_R^Y values, with cascade lasing at $3.3 \mu\text{m}$.

Fig. 7 (top), $T_{3\text{dB}}$ is very similar to that in the case with ESA until MIR emission starts, then it experiences a temporary dip, and eventually improves when Th^{MIR} is reached for a sufficiently wide yellow range. The tunability improvement provided by cascade lasing is limited, as $T_{3\text{dB}}$ values are still lower than those obtained in the absence of ESA. This is due to the non-uniform gain in the yellow wavelength range, which decreases as λ_s^Y deviates from λ_{peak}^Y . To give more insights on $P_o^R(\lambda_s^Y)$ versus λ_s^Y , the results for $P_i^F(\lambda_p)$ at 1 W and 4 W are reported in Figs. 8 and 9.

B. Pump Power Near the MIR Threshold

Laser behaviour for $P_i^F(\lambda_p) = 1 \text{ W}$ is depicted in Fig. 8 (bottom) in the cases with (a) and without (b) ESA, and with cascade lasing (c) to mitigate its effects. For each R_R^Y value, results are shown for an optimum length that is the average of L_{opt} values within $T_{3\text{dB}}$, which are shown in Fig. 8 (top). Notice that cascade lasing reduces L_{opt} compared to the cases with and without ESA. Being the considered $P_i^F(\lambda_p)$ close to Th^{MIR} , L_{opt} deviates from that in the case with ESA only when Th^{MIR} is reached, as is shown by the dip in the curves for R_R^Y equal to 60% or 70%. Since Th^{MIR} becomes higher when R_R^Y decreases, and it increases with λ deviation from λ_{peak}^Y , the dip in the L_{opt} curve

affects a larger portion of $T_{3\text{dB}}$ as R_R^Y increases, reaching the entire tunability range for $R_R^Y = 90\%$. The reduction in L_{opt} when cascade lasing is enabled is due to two reasons. Firstly, when the input pump power is close to Th^{MIR} , L_{opt} approaches that of MIR emission, reducing Th^{MIR} and thus improving yellow emission in advance. Once MIR emission begins, there is no need for L_{opt} to increase to counteract saturation, as MIR emission mitigates it, making the optimal length lower than in both cases with and without ESA. Fig. 8 (bottom) highlights that, as the considered $P_i^F(\lambda_p)$ is very similar to Th^{MIR} , the improvement in $P_o^R(\lambda_s^Y)$ given by cascade lasing is barely noticeable and limited to high R_R^Y values only. In fact, the best output power improvement in the presence of cascade lasing is just 12% compared to the case with ESA, being $P_o^R(\lambda_s^Y)$ equal to 232 mW and 206 mW when R_R^Y is 90%. The output power without ESA when $R_R^Y = 90\%$ is still 15% higher, being $P_o^R(\lambda_s^Y) = 265 \text{ mW}$.

C. Pump Power Above the MIR Threshold

Fig. 9 (bottom) depicts laser performance when the input pump power is $P_i^F(\lambda_p) = 4 \text{ W}$. As shown by L_{opt} values in Fig. 9 (top), differently from what is reported in Fig. 8 (top), in a situation of high input power cascade lasing provides a more significant reduction of L_{opt} for every R_R^Y value, as the laser operates well above Th^{MIR} . L_{opt} remains relatively similar to that for $P_i^F(\lambda_p) = 1 \text{ W}$ when Th^{MIR} is fully surpassed, especially for $R_R^Y = 90\%$. Moreover, the tuning range improves, due to cascade lasing, with respect to the case with ESA, particularly on the left-hand spectrum, but still falls short compared to the situation without ESA. As $P_i^F(\lambda_p)$ is way above Th^{MIR} , the improvement given by cascade lasing in terms of $P_o^R(\lambda_s^Y)$ is now appreciable. Fig. 8 (bottom) shows that the output power of the yellow laser is improved, regardless of R_R^Y , with respect to the case with ESA, eventually surpassing that obtained in its absence, especially at high R_R^Y values. In fact, the highest output power value in the presence of cascade lasing is just about 5% lower compared to the case without ESA, being 2 W and 2.1 W, respectively, when R_R^Y is 20%. Moreover, the best output power improvement provided by cascade lasing is as high as 55% and 23% compared to the case with and without ESA, respectively, when R_R^Y is 90%. In this situation, cascade lasing provides $P_o^R(\lambda_s^Y) = 1.07 \text{ W}$ whereas the maximum output power is 689 mW and 872 mW, respectively, in the other two

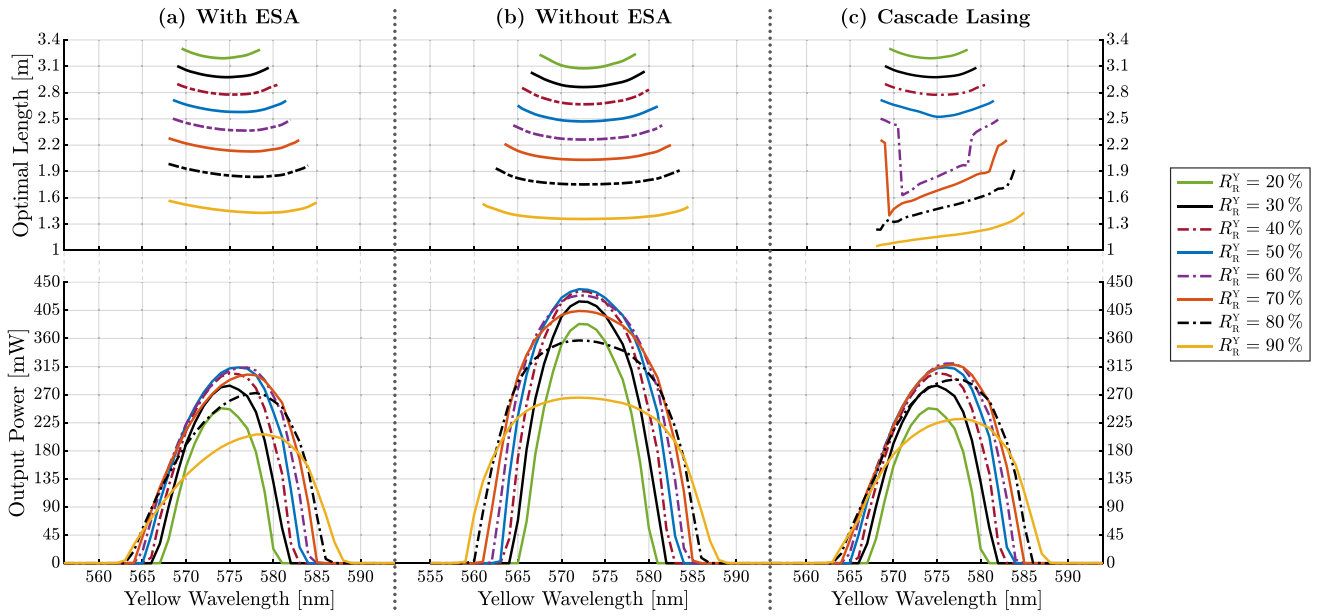


Fig. 8. Optimal fiber length in the 3-dB tunability range (top) and output power $P_o^R(\lambda_s^Y)$ (bottom) as a function of the lasing wavelength for various R_R^Y values. Input pump power $P_i^F(\lambda_p)$ is 1 W. The cases with (a) and without (b) ESA are compared with the cascade lasing one (c).

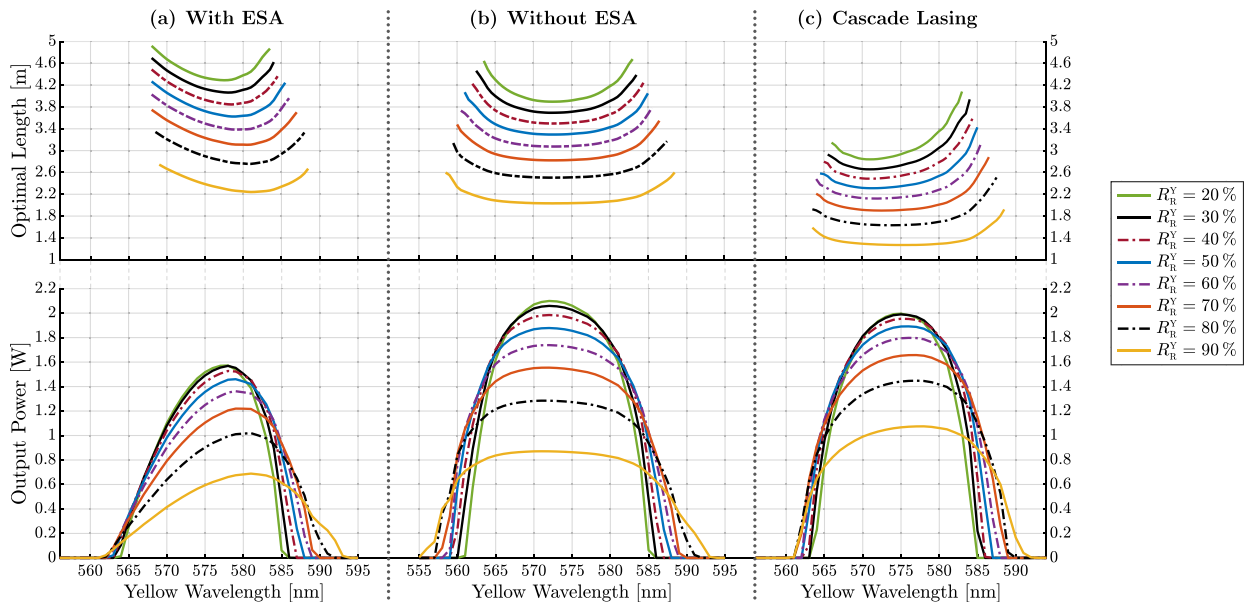


Fig. 9. Optimal fiber length in the 3-dB tunability range (top) and output power $P_o^R(\lambda_s^Y)$ (bottom) as a function of the lasing wavelength for various R_R^Y values. Input pump power $P_i^F(\lambda_p)$ is 4 W. The cases with (a) and without (b) ESA are compared with the cascade lasing one (c).

cases. This demonstrates that at high input pump power, the output power enhancement offered by cascade lasing exceeds expectations. The laser tuning range improvement is significant compared to the ESA case. However, the performance obtained when ESA is disabled is not overcome.

VI. CONCLUSION

In this work, we have conducted a comprehensive analysis of the influence of cascade lasing on both the output power and

the tunability of yellow lasers based on a Dy-doped ZBLAN fiber. Our simulation results provide useful insights for optimizing these visible FLs by properly designing the MIR cavity and selecting the optimal output mirror reflectivity and fiber length. Our study has revealed a strict relationship between R_R^Y and L , demonstrating a trade-off between output power and tuning range. Moreover, our in-depth analysis of cascade lasing shows its positive impact, mitigating the negative effect of ESA, while effectively avoiding saturation at high input pump power levels, suggesting possible performance enhancements

beyond the bounds of prior studies regarding ESA. This research contributes to a better understanding of the yellow FL design and highlights the potential of Dy:ZBLAN fibers for yellow emission via MIR cascade lasing, promising exciting opportunities for future experiments in this area.

REFERENCES

- [1] Y. Cai, J. Ding, Z. Bai, Y. Qi, Y. Wang, and Z. Lu, "Recent progress in yellow laser: Principles, status and perspectives," *Opt. Laser Technol.*, vol. 152, pp. 1–13, Aug. 2022.
- [2] X. Huo et al., "Research development of 589 nm laser for sodium laser guide stars," *Opt. Lasers Eng.*, vol. 134, Nov. 2020, Art. no. 106207.
- [3] E.-E. M. Mohamed, A.-K. H. Younes, and G. M. Hussein, "Efficacy of 577 nm pro-yellow laser in the treatment of melasma: A prospective split-face study," *J. Cosmet. Laser Ther.*, vol. 22, pp. 107–110, Mar. 2020.
- [4] C. F. Blodi, S. R. Russell, J. S. Pulido, and J. C. Folk, "Direct and feeder vessel photocoagulation of retinal angiomas with dye yellow laser," *Ophthalmol.*, vol. 97, no. 6, pp. 791–797, Jun. 1990.
- [5] A. H. Abd Elhamid, "Subthreshold micropulse yellow laser treatment for nonresolving central serous chorioretinopathy," *Clin. Ophthalmol.*, vol. 9, pp. 2277–2283, Dec. 2015.
- [6] K. Aflalo, M. Ben-David, A. Stern, and I. Juwiler, "Theoretical investigation of using a yellow (577 nm) laser for diabetic retinopathy," *OSA Continuum*, vol. 3, no. 11, pp. 3253–3266, Nov. 2020.
- [7] H.-H. Chen et al., "High beam quality yellow laser at 588 nm by an intracavity frequency-doubled composite Nd:YVO₄ Raman laser," *Opt. Exp.*, vol. 31, no. 5, pp. 8494–8502, Feb. 2023.
- [8] J. Liu et al., "Gan-based blue laser diodes with 2.2 W of light output power under continuous-wave operation," *IEEE Photon. Technol. Lett.*, vol. 29, no. 24, pp. 2203–2206, Dec. 2017.
- [9] M. Poulain, S. Cozic, and J. L. Adam, "Fluoride glass and optical fiber fabrication," in *Mid Infrared Fiber Photonics* (Woodhead Publishing Series in Electronic and Optical Materials), S. Jackson, M. Bernier, and R. Vallee, Eds., Woodhead Publishing, 2022, ch. 2, pp. 47–109.
- [10] F. Gan, "Optical properties of fluoride glasses: A review," *J. Non-Cryst. Solids*, vol. 184, pp. 9–20, May 1995.
- [11] A. Annunziato, F. Anelli, P. L. P. D. Teilleul, S. Cozic, S. Poulain, and F. Prudenzeno, "Fused optical fiber combiner based on indium fluoride glass: Perspectives for mid-IR applications," *Opt. Exp.*, vol. 30, no. 24, pp. 44160–44174, Nov. 2022.
- [12] A. Fuerbach, G. Bharathan, and M. Ams, "Grating inscription into fluoride fibers: A review," *IEEE Photon. J.*, vol. 11, no. 5, Oct. 2019, Art. no. 7103811.
- [13] L. Chen et al., "High-quality fiber bragg grating inscribed in ZBLAN fiber using femtosecond laser point-by-point technology," *Opt. Lett.*, vol. 47, no. 14, pp. 3435–3438, Jul. 2022.
- [14] Y. Ososkov, J. Lee, T. T. Fernandez, A. Fuerbach, and S. D. Jackson, "High-efficiency fluoroindate glass fiber laser," *Opt. Lett.*, vol. 48, no. 10, pp. 2664–2667, May 2023.
- [15] Y. Ososkov, J. Lee, T. T. Fernandez, A. Fuerbach, and S. D. Jackson, "FBG-stabilized dysprosium: fluoroindate mid-infrared fiber laser," in *Proc. CLEO/Europe-EQEC*, 2023.
- [16] R. I. Woodward, M. R. Majewski, G. Bharathan, D. D. Hudson, A. Fuerbach, and S. D. Jackson, "Watt-level dysprosium fiber laser at 3.15 μm with 73 % slope efficiency," *Opt. Lett.*, vol. 43, no. 7, pp. 1471–1474, Apr. 2018.
- [17] Z. Amin, M. Majewski, R. Woodward, A. Fuerbach, and S. D. Jackson, "Novel near-infrared pump wavelengths for dysprosium fiber lasers," *J. Light. Technol.*, vol. 38, no. 20, pp. 5801–5808, Oct. 2020.
- [18] M. R. Majewski, R. I. Woodward, and S. D. Jackson, "Dysprosium mid-infrared lasers: Current status and future prospects," *Laser Photon. Rev.*, vol. 14, no. 3, Feb. 2020, Art. no. 1900195.
- [19] Y. Wang et al., "Mid-IR tunable CW and passively Q-switched laser operation of Dy-doped fluoride fiber," *Opt. Mater. Exp.*, vol. 12, no. 4, pp. 1502–1511, Apr. 2022.
- [20] A. M. Loconsole, M. C. Falconi, A. Annunziato, S. Cozic, S. Poulain, and F. Prudenzeno, "Design of a Mid-IR laser based on a Ho:Nd-codoped fluoroindate fiber," *J. Light. Technol.*, vol. 41, no. 2, pp. 702–708, 2023.
- [21] M. C. Falconi, A. M. Loconsole, A. Annunziato, S. Cozic, S. Poulain, and F. Prudenzeno, "Design of a broadband erbium-doped fluoroindate fiber laser emitting up to 3.91 μm ," *J. Light. Technol.*, vol. 41, no. 18, pp. 6065–6072, 2023.
- [22] M. Amin, S. D. Jackson, and M. Majewski, "Experimental and theoretical analysis of Dy³⁺ doped fiber lasers for efficient yellow emission," *Appl. Opt.*, vol. 60, no. 16, pp. 4613–4621, Jun. 2021.
- [23] J. Zou et al., "Direct generation of watt-level yellow Dy³⁺-doped fiber laser," *Photon. Res.*, vol. 9, no. 4, pp. 446–451, Apr. 2021.
- [24] H. Wang et al., "High-efficiency, yellow-light Dy-doped fiber laser with wavelength tuning from 568.7 to 581.9 nm," *Opt. Lett.*, vol. 44, no. 17, pp. 4423–4426, Jul. 2019.
- [25] R. Piramidowicz, M. Klimczak, and M. Malinowski, "Short-wavelength emission analysis in Dy:ZBLAN glasses," *Opt.*, vol. 30, no. 5, pp. 707–710, Jan. 2008.
- [26] M. Federico and F. Poli, "Numerical optimization of tunable Dy-doped ZBLAN fiber lasers for yellow emission," in *Proc. Specialty Opt. Fibres*, 2023, Art. no. 125730B.
- [27] M. Federico and F. Poli, "Cascade lasing optimization in Dy-doped ZBLAN fiber lasers for efficient yellow emission," in *Proc. CLEO/Europe-EQEC*, Jun. 2023, p. 14.
- [28] R. I. Woodward and M. Gorjan, "Modeling mid infrared fiber laser systems," in *Mid Infrared Fiber Photonics* (Woodhead Publishing Series in Electronic and Optical Materials), S. Jackson, M. Bernier, and R. Vallee, Eds., Woodhead Publishing, 2022, ch. 13, pp. 743–801.
- [29] E. Desurvire, *Erbium-Doped Fiber Amplifiers: Principles and Applications*. Hoboken, NJ, USA: Wiley, 2002.
- [30] D. Marcuse, "Gaussian approximation of the fundamental modes of graded-index fibers," *J. Opt. Soc. Am.*, vol. 68, pp. 103–109, Aug. 1977.

Michelangelo Federico (Graduate Student Member, IEEE) received both the bachelor's degree in electronics, informatics, and telecommunications eEngineering and master's degree in communication engineering from the University of Parma, Parma, Italy, in 2019 and 2022, respectively. He working toward the Ph.D. degree in information technology with the homonymous University, specializing in the numerical modeling of fiber-based lasers and amplifiers. His research interests include the optimization of yellow emission, along with the analysis of bismuth-doped fiber amplifiers for the next generation of ultra-wideband optical communications.

Federica Poli (Member, IEEE) was born in 1977. She received the Laurea (*cum laude*) degree in electronic engineering and Ph.D. degree in information technology from the University of Parma, Parma, Italy, in 2002 and 2006, respectively. Since 2006, she has been with the Information Engineering Department, University of Parma. She is currently an Associate Professor with the Department of Engineering and Architecture, University of Parma. Her research interests include specialty fibers and photonic crystal fibers, optical fiber lasers and amplifiers, and numerical methods for electromagnetic field analysis.